Viscous Flow Simulation of the HART II Rotor Using Unstructured Adaptive Meshes

Dong Ok Yu* and Oh Joon Kwon†

Korea Advanced Institute of Science and Technology (KAIST)
335 Gwahak-ro,Yuseong-gu, Daejeon 305-701, KOREA

Abstract

In the present study, viscous flow simulations of the HART II rotor were conducted using a flow solver based on unstructured meshes. To capture the blade-vortex interaction (BVI) phenomena accurately and to resolve the near wake effectively in descending flight, a series of solution-adaptive mesh refinements was carried out. Combination of an overset mesh method and a deforming mesh technique was used to handle relative blade motion involving blade rotation in the azimuthal direction, input pitch control, and elastic blade deformation. In the present study, the blade deformation was prescribed from the HART II rotor measurement. Calculations were made for two configurations, isolated rotor and rotor-fuselage configuration, to investigate the fuselage effect on the blade loading and the rotor wake structure. It was found that inclusion of fuselage makes significant improvement in the trim control prediction, which results from the more accurate prediction of rotor inflow at the front and rear portions of the rotor disk. This improved trim control also leads to an improvement in the blade loading prediction for the rotor-fuselage configuration. From the solution-adaptive mesh refinement study, it was found that high frequency blade loading caused by BVI can be obtained more accurately as the mesh is further refined, whereas the low frequency loading is mostly independent to the mesh resolution. It was also found that to predict the unsteady time-accurate solution, such as the high frequency BVI loading, accurately, the blade rotation should be made with a proper azimuth angle increment equivalent to local cell size. The predicted vortex core positions at the retreating side of the rotor are well matched with measurement, whereas relatively large difference between the prediction and the measurement was observed at the advancing side.

Nomenclature

c	chord length
r	radial position
R	rotor radius
α_s	shaft angle, positive aft
C_T	rotor thrust
θ_0	collective pitch angle
θ_{1c}	lateral cyclic pitch angle
θ_{1s}	longitudinal cyclic pitch angle
ψ	azimuth angle
w	velocity component in z-direction
M	Mach number
F_n	normal force
a	speed of sound
ρ	density
C_nM^2	sectional normal force coefficient $= \frac{F_n}{1/2\rho a^2 c}$

* Graduate Research Assistance, Department of Aerospace Engineering

† Corresponding Author, Professor, Department of Aerospace Engineering, E-mail: ojkwon@kaist.ac.kr

1. Introduction

Until recently, unsteady flow simulation of a helicopter rotor remains one of the most challenging problems in the field of applied aerodynamics. For the prediction of rotor blade loading, unsteadiness of the flow field should be accurately simulated. At the same time, the simulation must account for the blade structural dynamic deformation, since rotor blades are not structurally stiff. In forward flight, rotor trim must also be achieved to satisfy the trim targets involving rotor thrust, pitching moment, and rolling moment. Also, the effect of rotor-fuselage interaction may be non-negligible in certain flight conditions. In this regard, for solving the rotor flow problems, a complete and comprehensive simulation is required, along with the ability of handling complex geometries and predicting rotor wake accurately.

In the past decades, a series of experimental studies were conducted by the international collaboration between German DLR, French ONERA, NASA Langley, Netherlands DNW, and the US Army Aeroflightdynamics Directorate, to investigate the influence of higher-harmonic control (HHC) on blade-vortex interaction (BVI) in descending flight, which is known as the HART (Higher Harmonic Control Aeroacoustics Rotor Test) program. In 1994, the HART I test [1] was initiated with a 40% Mach-scaled model rotor of a BO105 main rotor. In the tests, blade loading, acoustic signature, and blade deformation were measured, but little information was obtained regarding the rotor wake structure. As an extension of the HART I tests, the HART II tests [2, 3] were conducted later to focus more on investigating the wake structure. In the HART II tests, three different flight conditions were considered: a baseline (BL) case with conventional control inputs, and two additional cases with higher harmonic control inputs for minimum-vibration (MV)

and minimum-noise (MN) cases. The measured data includes blade loading, acoustic signature, blade deformation, and wake structure. Since blade loading and noise are closely related with the wake structure and the blade deformation, this complete database is extremely useful for validating comprehensive analysis tools.

Previously, several numerical studies were conducted to simulate the BVI phenomena and the wake structure of the HART II rotor tests. Lim [4] performed a comprehensive analysis by using a coupled OVERFLOW-2/CAMRADII code. For the wake prediction, a high-order WENOM scheme was used with 35.5M grid points. In this study, blade loading and blade deformation were also calculated, including the effect of fuselage. The results showed that the blade loading is largely affected by the rotational flow behind the rotor hub. Boyd [5] also used the same OVERFLOW-2/CAMRADII code, but the number of grid points was increased to about 69M. This study was focused more on acoustic problems related to BVI, as well as blade loading. Biedron and Lee-Rausch [6] used a coupled FUN3D/CAMRADII approach. The FUN3D code is based on unstructured meshes, and preserves a second order of accuracy in space. The simulation was made with 13.6M grid points which were clustered in the near wake region. The blade loading was predicted reasonably well, but the peak-to-peak variation of the BVI loading was relatively small compared to the previous OVERFLOW-2 results. Yang and Aoyama [7] used an Euler flow solver with a fourth-order compact MUSCL TVD scheme. The number of grid points used was nearly 41M grid points, and the blade deformation was taken from the HART II measurement. Although viscosity was not included, the results of blade loading were reasonably good. The effect of fuselage on the blade loading was also considered, but was not discussed in detail.

In the present study, viscous flow simulations of the HART II rotor baseline (BL) case were conducted. The test configurations and the computational domain were modeled using unstructured meshes so that complex geometries can be easily handled. A solution-adaptive mesh refinement technique was also adopted to resolve the tip vortex better and to capture the BVI loading more accurately. The blade deformation was prescribed from the HART II measured data. Calculations were made for both isolated-rotor and rotor-fuselage configurations to investigate the effect of fuselage on the rotor blade loading and the wake structure. The effects of time step size and mesh refinement were also examined. For validation, the results are compared with the experimental data.

2. Numerical Method

In the present study, an unstructured mesh CFD flow solver [8, 9] was used for the simulation of unsteady time-accurate viscous flows around the HART II rotor. The governing Reynolds-Averaged Navier-Stokes equations were discretized using a vertex-centered finite-volume method. The flow domain was divided into a finite number of control volumes composed of median duals surrounding each vertex. The inviscid flux terms were computed using Roe's flux-difference splitting scheme. The flow variables at each dual face were computed by using a linear reconstruction approach to achieve second-order spatial accuracy. The second-order derivatives of the viscous terms were evaluated by using the Green-Gauss theorem, and the viscous flux terms were computed by adopting a modified central differencing. An implicit time integration algorithm based on a linearized second-order Euler backward difference was used to advance the solution in time. The linear system of equations was solved at each time step using a point Gauss-Seidel method. The Spalart-Allmaras one-equation turbulence model was adopted to estimate the eddy viscosity. To reduce the large computational time, a parallel algorithm based on a domain decomposition strategy was adopted. The load balancing between processors was achieved by partitioning the global computational domain into local subdomains using the MeTiS libraries. The Message Passing Interface was used to transfer the flow variables across the subdomain boundaries. All calculations were performed on PC-based Linux clusters.

3. HART II Model

The HART II experiments [2] used a 40% Mach-scaled, four-bladed, hingeless BO105 model rotor. The rotor blades are rectangular with -8° linear twist and a precone angle of 2.5°. The blade features a modified NACA23012 airfoil with a trailing-edge tab of 5.4 mm length and 0.8 mm thickness. The rotor was installed with the rotor shaft angle of 5.3° (nose-up) that was designed to simulate a descending flight. In the present calculations, the rotor shaft angle of 4.5° was used for the correction of the wind tunnel wall effects. The test conditions are summarized in Table1.

In the present study, two computational configurations were considered. The first one is isolated-rotor configuration, and the second one is rotor-fuselage configuration to investigate the effect of fuselage on the blade loading and the rotor wake. In the case of the isolated rotor, the blade root was cut at the radial location of 0.44m from the hub center. For the rotor-fuselage configuration, the blade root was extended further inboard to 0.198m from the hub center to realistically model the HART II experimental configuration. The solid modeling of the two configurations is presented in Fig. 1.

Table 1. HART II test conditions [2].

Rotor radius, R	2.0 m
Blade chord length, c	0.121 m
Twist angle	-8.0°
Precone angle, β_p	2.5°
Thrust coefficient, C_T	0.0044
Advance ratio, μ	0.15
Shaft angle, α_s	4.5° (aft)
Tip Mach number	0.6387

4. Blade Deformation

In the present study, the blade motion was prescribed based on a variable-separable interpolation of the blade deflections that were measured at discrete azimuthal and radial locations of each blade. The deflection, D, can be reconstructed by using an interpolating function as

$$D(r,\psi) = \sum_{i=1}^{N_r} \sum_{j=1}^{N_a} a_{ij} R_i(r) P_j(\Psi) \qquad (1)$$

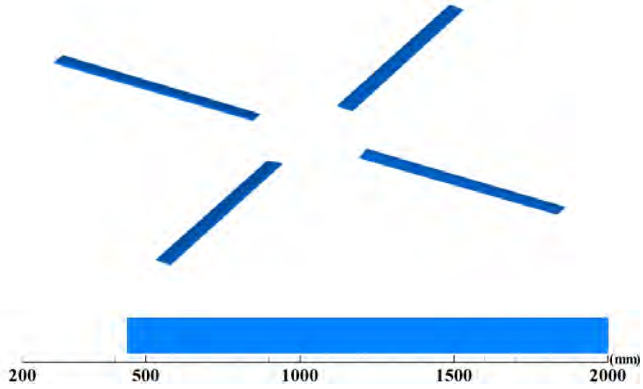

(a) Isolated-rotor configuration

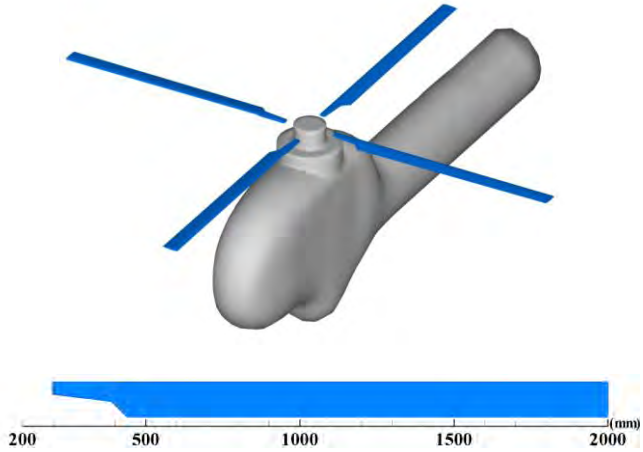

(b) Rotor-fuselage configuration

Figure 1: Computational models and blade planform shape.

where r is the non-dimensional radial coordinate, and ψ is the azimuth angle. N_r and N_a are the number of radial and azimuthal interpolation functions, respectively, and $R_i(r)$ and $P_j(\psi)$ are used to describe the blade deflection. The radial interpolation functions are taken to be polynomials, and the azimuthal interpolation functions are taken to be the components of a Fourier series:

$$R_i(r) = r^{(i-1)} \tag{2}$$

$$P_j(\psi) = \begin{cases} \cos\dfrac{j-1}{2}\psi & if \quad j \in \{1,3,5.....\} \\ \sin\dfrac{j}{2}\psi & if \quad j \in \{2,4,6.....\} \end{cases} \tag{3}$$

The coefficients a_{ij} of the interpolation function are obtained using a simple least squares fitting, and the set of coefficients are given in Ref. 10. In Fig. 2, the approximation of the blade torsion is compared with the measured data [3]. The maximum differences between the approximation and measurement are 0.5° and 0.5 mm for the torsion and the flap/lag, respectively [10].

5. Computational Mesh

In the present study, an unstructured overset mesh technique [11] was adopted to handle the relative motion between the blades and the fuselage. In this overset mesh scheme, the mesh topology is composed of multiple independent mesh blocks. The main background mesh

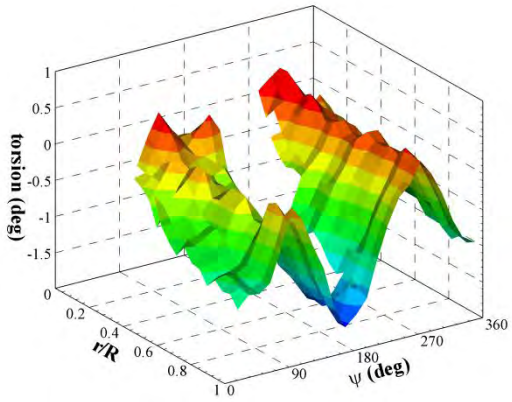

(a) Measurement [3]

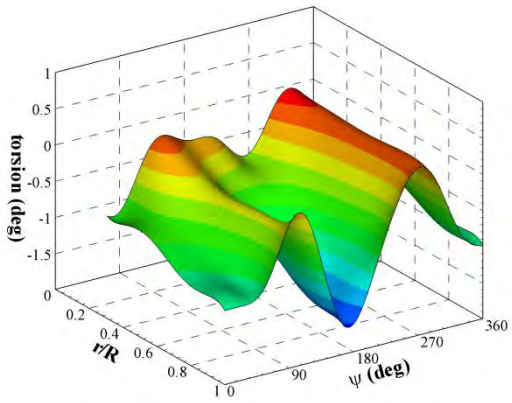

(b) Approximation

Figure 2: Comparison of blade torsion deformation between measured data and approximated interpolation.

represents the complete computational domain and contains the fuselage, and the sub-block meshes cover each individual blade. To resolve the boundary layer on the blade and fuselage surfaces, a hybrid mesh topology containing both prismatic and tetrahedral cells was used. The mesh deformation at every time step due to blade deformation was taken care of by using a spring analogy [12, 13] and an algebraic method [14], which were applied to tetrahedral elements in the far-field region and to the prismatic elements inside the boundary layer, respectively.

A solution-adaptive mesh refinement technique was adopted to effectively resolve the tip vortex. The mesh adaptation was applied in a quasi-unsteady manner to avoid excessive computational overhead typically accompanied when the mesh adaptation is applied in a fully unsteady dynamic manner, particularly in 3-D. In the present approach, cells carrying high vorticity level are tagged at every time step as the blades rotate. Once the rotor completes one period of rotation, the calculation is paused and the tagged cells are refined. In the present study, two levels of mesh adaptation were made.

Figures 3 and 4 show computational meshes after each level of mesh adaptation for both isolated-rotor and rotor-fuselage configurations. As shown in these figures, the mesh refinement is mostly concentrated in the vicinity of the rotor disk, and the cell size in the wake region decreases as the mesh refinement proceeds. For both configurations, the typical cell size in the wake region corresponds to 0.25c for the initial meshes and 0.125c for the meshes after the first level mesh adaptation, where c is chord length. After the second level adaptation, the cell size was further reduced to approximately 0.0625c. The typical size of the computational cells and the mesh resolution for both

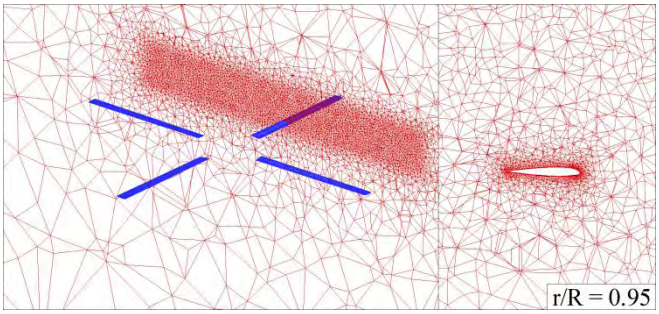

(a) Initial mesh

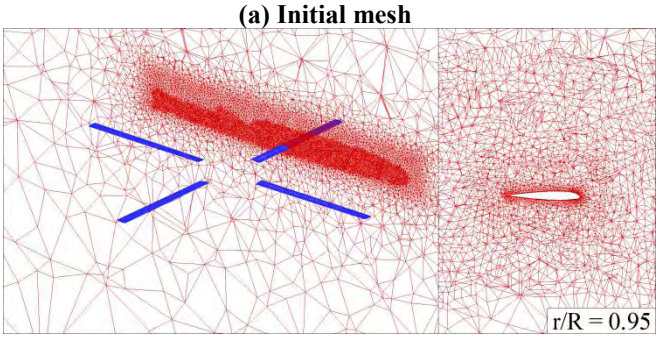

(b) First-level adaptation

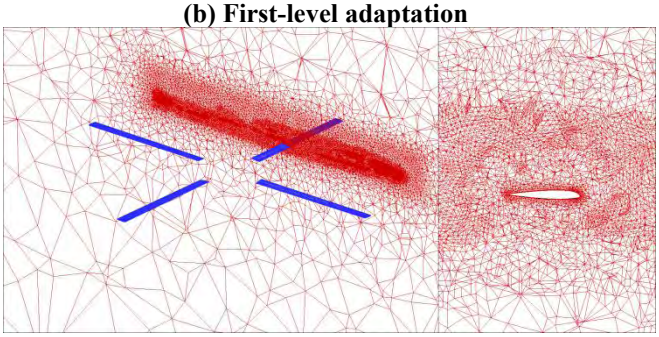

(c) Second-level adaptation

Figure 3: Computational meshes after each level of mesh adaptation for isolated- rotor configuration.

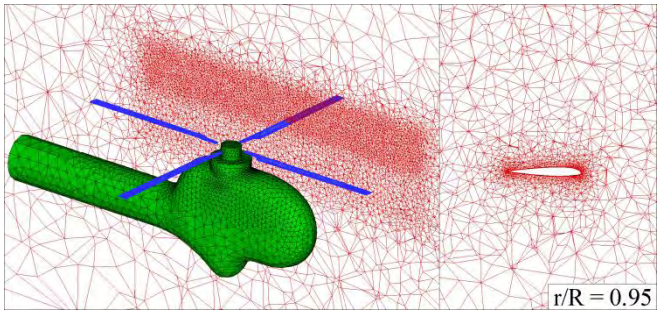

(a) Initial mesh

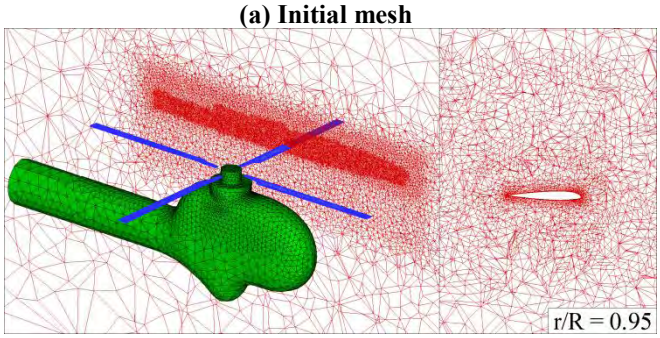

(b) First-level adaptation

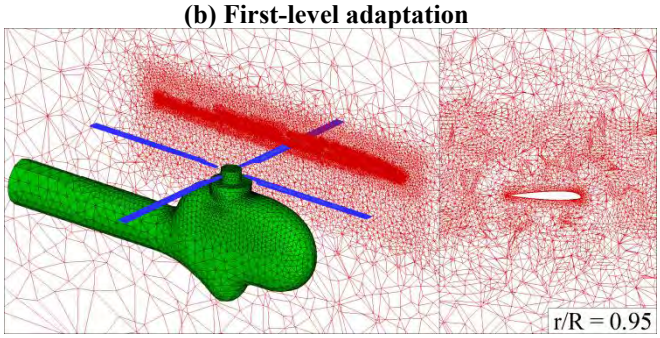

(c) Second-level adaptation

Figure 4: Computational meshes after each level of mesh adaptation for rotor-fuselage configuration.

configurations were kept very similar to each other to avoid the dependency of the predicted results on the cell size. The detailed information about the meshes used is summarized in Table 2. The additional number of nodes and cells after including the fuselage is due to the addition of prismatic cells surrounding the fuselage.

Table 2. Meshes after each level of adaptation.

		Isolated-rotor	Rotor-fuselage
Initial mesh	nodes	2,897,615	3,030,066
	cells	9,043,189	9,668,173
First-level adaptation	nodes	4,451,881	4,545,440
	cells	18,210,699	18,569,101
Second-level adaptation	nodes	8,042,165	8,660,890
	cells	39,416,933	42,928,170

6. Results and Discussion

6.1 Rotor Trim

In order to retain the predicted thrust to a desired level and to eliminate rotor aerodynamic moments, a rotor trim procedure was applied to both isolated-rotor and rotor-fuselage configurations. These trim calculations were performed on the initial meshes to avoid the excessive computational time involved in the trim cycles. The trim controls consist of collective (θ_0), lateral cyclic (θ_{1c}) and longitudinal cyclic (θ_{1s}) pitch angles, which are directly related to rotor thrust, pitching moment, and rolling moment, respectively. The trim state was obtained by adjusting the trim controls iteratively using a Newton-Raphson method [15]. One trim cycle consists of six rotor revolutions: three for calculating the derivatives of the force and moments with respect to the trim controls, and the remaining three for the solution iteration.

In Fig. 5, comparison of the trim controls between the prediction and the measured data [3] is presented. As shown in the figure, negligible difference was observed in the collective pitch angles between the isolated-rotor and rotor-fuselage configurations. In contrast, improved predictions of the cyclic pitch angles were obtained for the rotor-fuselage configuration over the isolated-rotor configuration, particularly for the lateral cyclic pitch angle θ_{1c}.

To better understand the effect of fuselage on the trim controls, rotor downwash and the airload distributions on the rotor were examined. In Fig. 6, the difference of the w-velocity component between the isolated-rotor and rotor-fuselage configurations ($\Delta w_{vel} = w_{rotor\text{-}fuselage} - w_{isolated\ rotor}$) on the cutting plane located 1.5c below the rotor disk plane is presented. It is shown that noticeable difference of w-velocity exists near the azimuth angles of 0° and 180°, indicating that the fuselage induces non-negligible upwash and downwash flows near 0° and 180° azimuth angles, respectively. Figure 7 shows comparison of the predicted

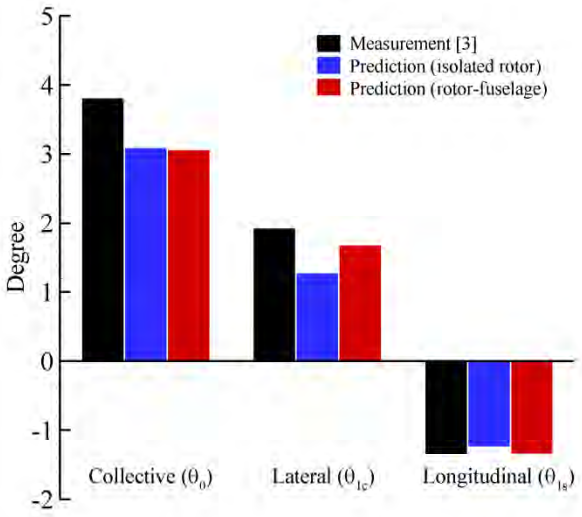

Figure 5: Comparison of predicted and measured [3] trim controls.

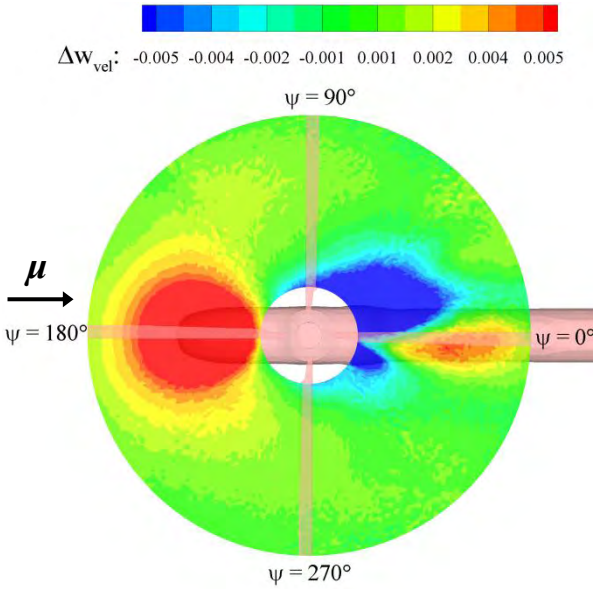

Figure 6: Difference of w-velocity component on the cutting plane located 1.5c below the rotor disk between isolated-rotor and rotor-fuselage configurations ($\Delta w_{vel} = w_{rotor\text{-}fuselage} - w_{isolated\ rotor}$).

streamline traces around the rotor and the fuselage between the isolated-rotor and rotor-fuselage configurations. It is shown that due to the blockage of the fuselage, the flow is deflected upward in front of the rotor hub and in the downward direction behind the hub. These upward and downward flows around the fuselage effectively change the local angle of attack of the rotor blades, and consequently influence the rotor blade loading.

Figure 8 shows the difference of the sectional normal force coefficient ($\Delta C_nM^2 = C_nM^2_{rotor\text{-}fuselage} - C_nM^2_{isolated\ rotor}$) between the isolated-rotor and rotor-fuselage configurations for one rotor revolution. To extract the pure fuselage effect, C_nM^2 from the rotor-fuselage configuration was computed with the same trim control settings as those of the isolated-rotor. It is shown that noticeable difference of C_nM^2 exists near the azimuth angles of 0° and 180° where the rotor downwash was most influenced by the existence of the fuselage as indicated in Fig. 7. Some additional loading differences is also observed at the advancing side. Because of this loading change, the rotor pitching and rolling moments increase, and

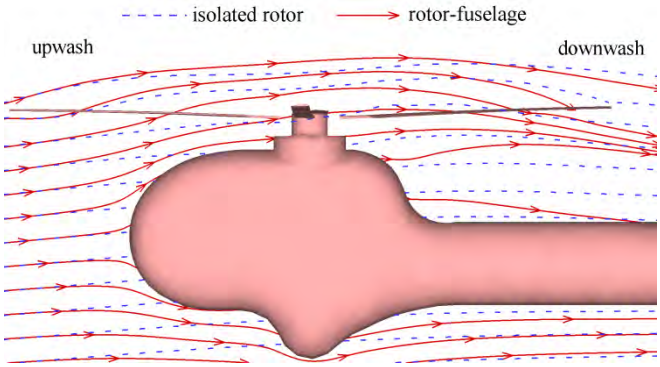

Figure 7: Comparison of streamline traces around the rotor and fuselage between isolated-rotor and rotor-fuselage configurations.

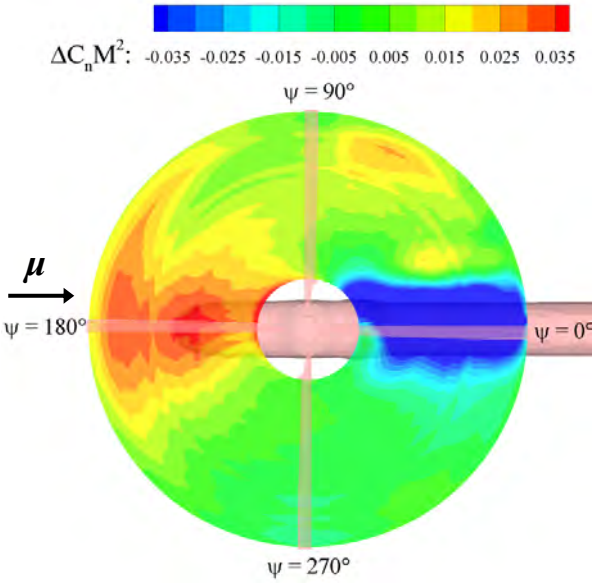

Figure 8: Difference of blade loading between isolated-rotor and rotor-fuselage configurations ($\Delta C_nM^2 = C_nM^2_{rotor\text{-}fuselage} - C_nM^2_{isolated\ rotor}$).

as a result, the cyclic pitch setting should also be increased in positive and negative directions, respectively, to further compensate these additional pitching and rolling moments in the case of the rotor-fuselage configuration.

6.2 Effect of Time Step Size

In rotor flow simulations, the time step size (or the azimuth angle increment in time) is one of the important fundamental parameters affecting the accuracy of the unsteady solutions. When smaller azimuth angle increment is used, more accurate results can be obtained, but the computational time becomes excessively large. In this section, a study to optimize the time step size was conducted. This test calculation was performed using four different azimuth angle increments, 1.0°, 0.5°, 0.25°, and 0.125°, for the isolated rotor configuration on the mesh obtained after the first adaptation. In Fig. 9, the sectional loading C_nM^2 at 87 % radial location is compared. As shown in the figure, non-physical oscillations of the blade loading were observed for the two relatively large time steps with the azimuth angle increments of 1.0° and 0.5°. In contrast, the predicted sectional loading becomes independent and shows a converged solution when the increment is smaller than 0.25°.

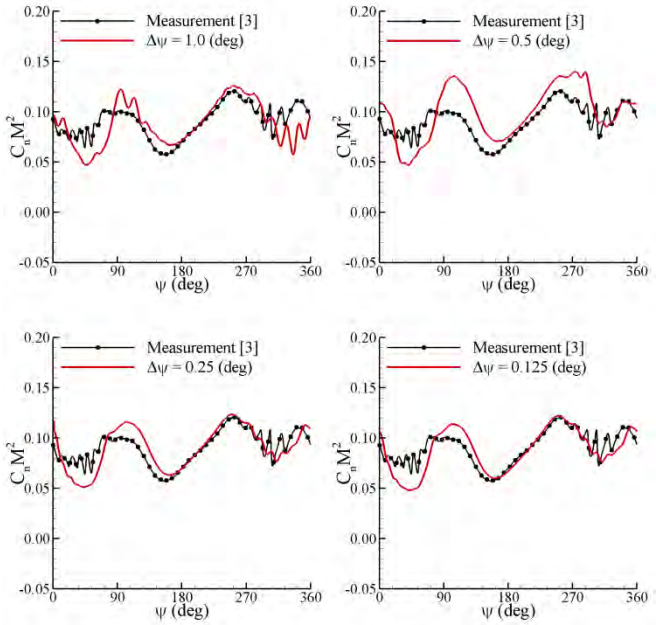

Figure 9: Effect of azimuth angle increment on C_nM^2 at 87 % radial location (isolated-rotor configuration).

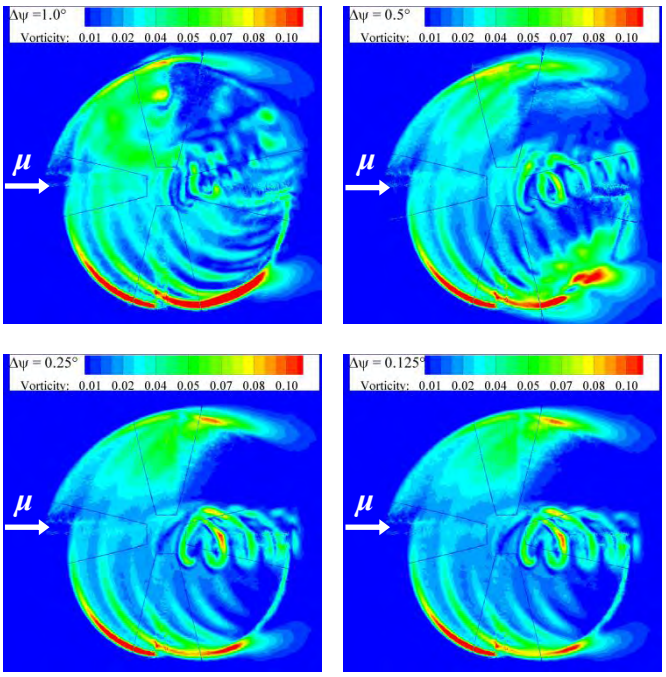

Figure 10: Effect of azimuth angle increment on vorticity field at the cutting plane located 1.0c above rotor disk plane (isolated-rotor configuration).

Figure 10 shows comparison of the vorticity field at the cutting plane located 1.0c above the rotor disk plane when the reference blade is located at the azimuth angle of 0°. The results also confirm that a converged solution is obtained for the time step size less than 0.25°. Based on these results, all calculations were performed by using the azimuthal angle increment of 0.25° for the first-level adaptation mesh. Similar tests were also conducted for the initial coarse mesh and the mesh after the second-level adaptation, and it was concluded that 0.5° and 0.125° increments are satisfactory for each mesh, respectively.

6.3 Effect of Mesh Adaptation

In the present study, a series of solution-adaptive mesh refinement were applied to capture the BVI loading accurately. In Fig. 11, the effect of adaptive mesh refinement on the blade loading at 87% radial location is presented for the rotor-fuselage configuration. The full signal of C_nM^2 in Fig. 11(a) shows that the loading below 3/rev variation is well predicted for all meshes, but the BVI loading at the 1st and 4th quadrants is strongly dependent on the level of mesh adaptation. To better understand the effect of mesh adaptation on the blade loading, the full signal of C_nM^2 is filtered to distinguish the high frequency components (> 7/rev) from the lower ones (0~7/rev). The high frequency loading is exclusively associated with BVI, while the low frequency loading is primarily associated with the control pitch angles and the blade structural deformation. In Fig. 11(b), comparison of the low frequency loading is presented. It is shown that the low frequency loading is mostly independent to mesh refinement. The predicted results compare very well with measurement [3] at the 3rd and 4th quadrants, but slightly under/over-predicted at the remaining quadrants. In Fig. 11(c), the high frequency loading is compared. For the initial mesh, the BVI loading at the 1st and 4th quadrants is not well captured due to the numerical dissipation for accurately capturing the rotor wake. In summary, as the computational mesh was further refined, the magnitude of high frequency loading was also amplified, even though the refinement was not still dense enough for capturing the BVI loading at the 4th quadrant.

Figure 12 shows comparison of the vorticity fields at the cutting plane located 1.0c above the rotor disk plane when the reference blade is at the azimuth angle of 0°. In the case of the initial mesh, the tip vortex at the front of the rotor disk is highly dissipated, indicating high numerical dissipation. It is shown that as the mesh is further refined, the tip vortex is better preserved. It is also shown that the tip vortex in the advancing side (1st and 2nd quadrants) is less well-defined than that in the retreating side (3rd and 4th quadrants), causing poor prediction of the BVI loading as shown in Fig. 11. It is known that prediction of BVI loading in the advancing side is usually more difficult, compared to the retreating side, because the tip vortex in the advancing side is inherently weaker due to the relatively small angle of attack of the blade. In addition, the age of the vortex in the advancing side is much older than that in the retreating side. In contrast, the rotor blades entering the 4th quadrant encounter relatively young and strong vortices.

Figure 13 shows the effect of adaptive mesh refinement on the leading-edge pressure difference ($\Delta P=P_{up}-P_{low}$) at 3% chordwise position for the rotor-fuselage configuration. The pressure difference was filtered to extract the components higher than 7/rev, and is plotted for one rotor revolution. Again, for the initial mesh, the stripe pattern at the 1st and 4th quadrants, which represents the BVI phenomena, is entirely missed. As the mesh is further refined, this stripe pattern becomes more distinctive.

6.4 Effect of Fuselage

To investigate the effect of fuselage on the blade loading, comparison of C_nM^2 between the isolated-rotor and rotor-fuselage configurations is made in Fig. 14. The results are presented after the second level mesh adaptation. It is shown that after the inclusion of the fuselage the predicted low

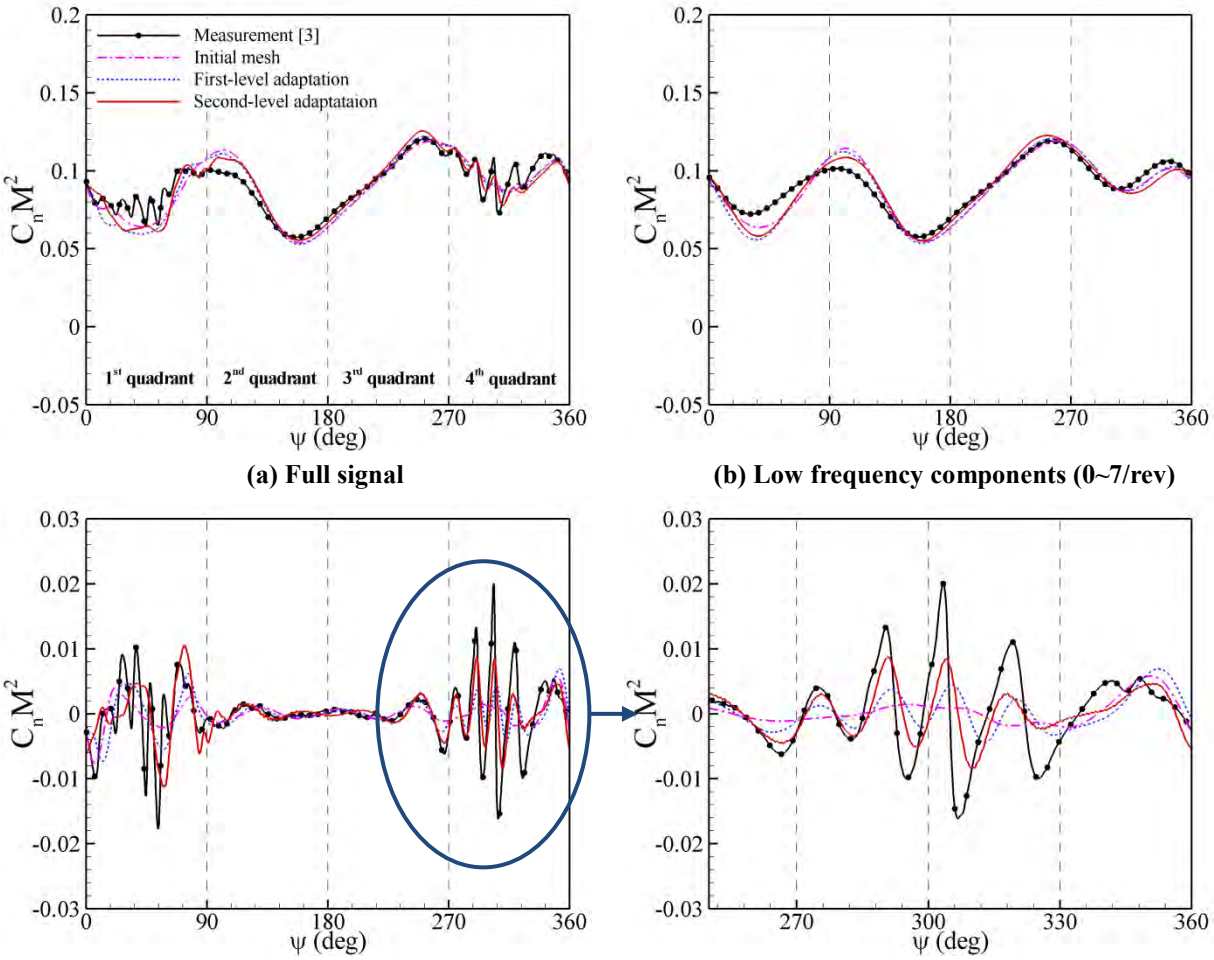

(a) Full signal **(b) Low frequency components (0~7/rev)**

(c) High frequency components (> 7/rev)

Figure 11: Effect of solution-adaptive mesh refinement on blade loading at 87 % radial location (rotor-fuselage configuration).

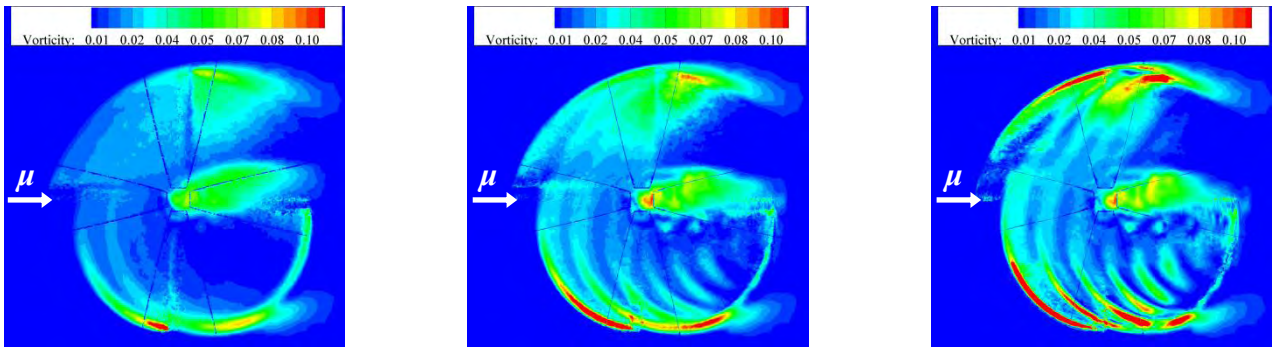

(a) Initial mesh **(b) First-level adaptation** **(c) Second-level adaptation**

Figure 12: Effect of solution-adaptive mesh refinement on vorticity field on cutting plane 1.0c above rotor disk plane (rotor-fuselage configuration).

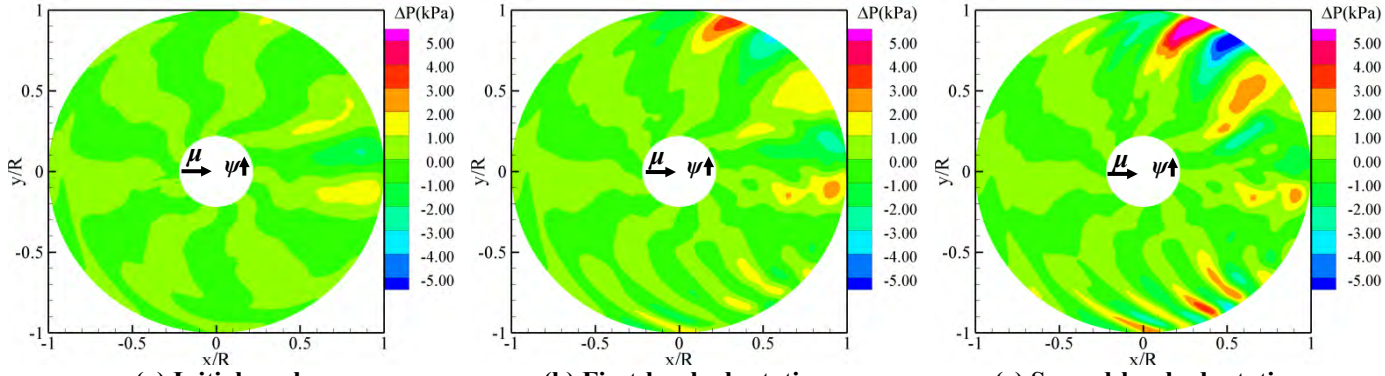

(a) Initial mesh **(b) First-level adaptation** **(c) Second-level adaptation**

Figure 13: Effect of solution-adaptive mesh refinement on high frequency components (>7/rev) of leading-edge pressure difference at 3% chordwise position of blade (rotor-fuselage configuration).

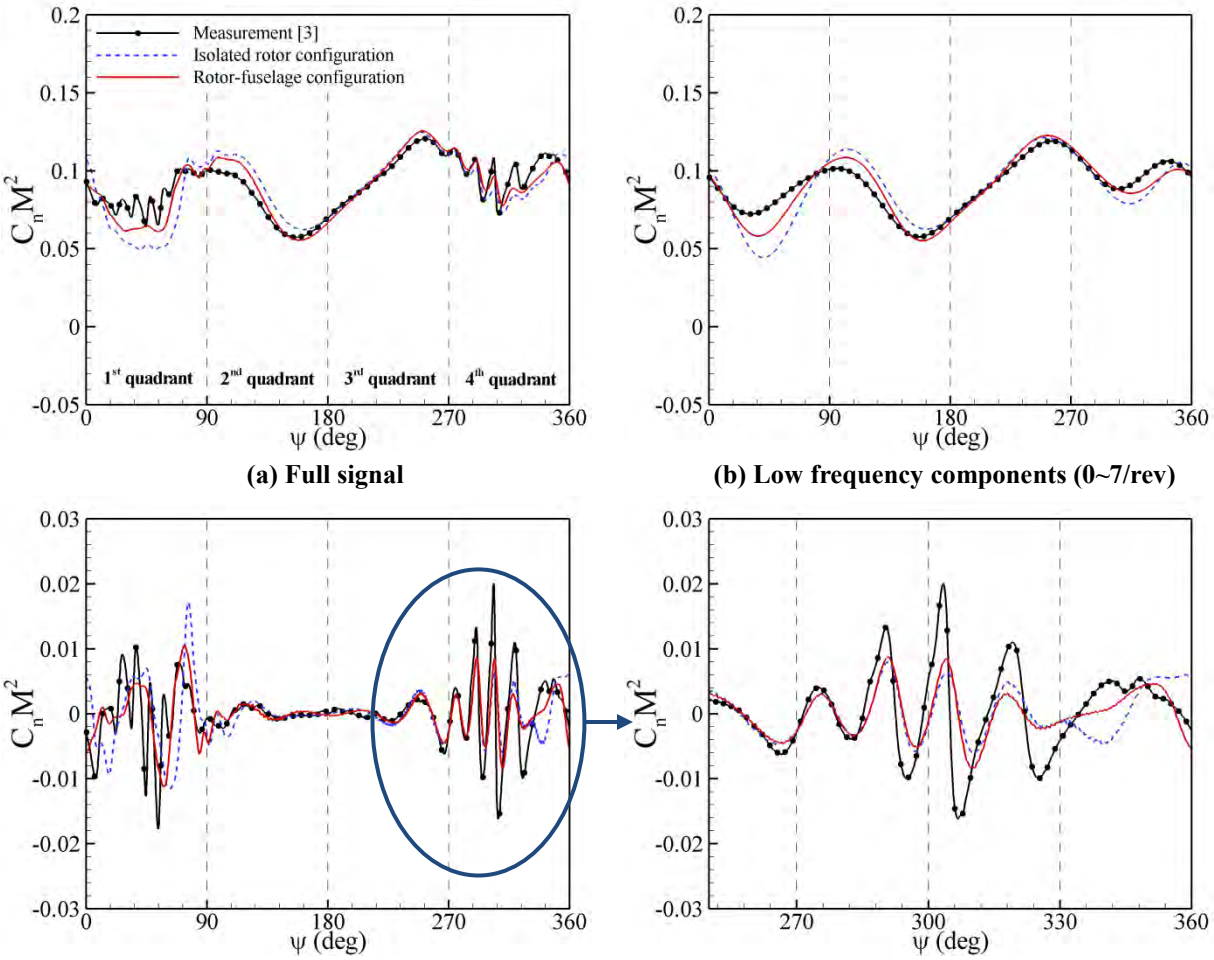

(a) Full signal **(b) Low frequency components (0~7/rev)**

(c) High frequency components (> 7/rev)

Figure 14: Comparison of C_nM^2 between isolated-rotor and rotor-fuselage configurations after second level of mesh adaptation.

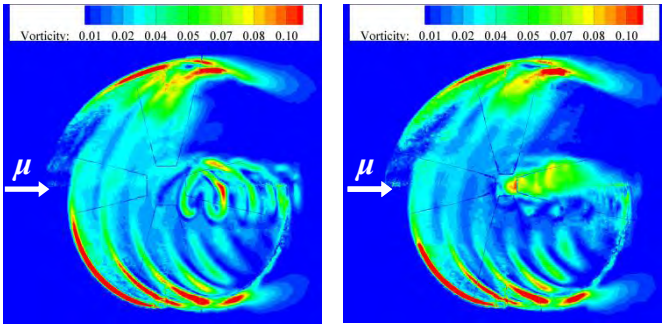

(a) Isolated-rotor configuration **(b) Rotor-fuselage configuration**

Figure 15: Comparison of vorticity fields 1.0c above rotor disk plane between isolated-rotor and rotor-fuselage configurations after second level mesh adaptation.

frequency loading is significantly improved at most of the azimuthal stations. This improvement is directly related to the improved prediction of trim controls and rotor inflow as described in Figs. 5 and 7. For the high frequency loading, local improvement in the blade loading near the azimuth angle of 360° is observed, which is mainly due to the different wake structures in that region between the two configurations.

In Fig. 15, the vorticity fields on the cutting plane 1.0c above the rotor disk plane are compared between the two configurations after the second-level mesh refinement when the reference blade is located at the azimuth angle of 0°. The figure shows that a strong and distinctive root vortex develops for the isolated-rotor configuration, while for the rotor-fuselage configuration a wake flow develops behind the rotor hub without a distinctive root vortex.

In Fig. 16, comparison of the leading-edge pressure difference for the two configurations with the measurement [3] is made for the results after the second-level mesh adaptation. It is shown that the overall accuracy of the prediction is improved by including the fuselage in the prediction, particularly near the azimuth angle of 0°. In the measurement, the stripe patterns from BVI at the 1st and 4th quadrants are clearly presented. These patterns are well predicted after the second-level mesh adaptation, even though the strength is slightly lower than the measurement. However, relatively poor prediction is observed in the first quadrant.

6.5 Tip Vortex Core Position

Figure 17 shows the rotor wake structure represented by the iso-surface of λ_2-criterion for the rotor-fuselage configuration after the second-level mesh adaptation. The figure is presented when the reference blade is located at the azimuth angles of 20° and 70°. In the figure, the selected vortex core positions on the longitudinal cutting planes located at y=1.4m and y=-1.4m are labeled consistently with the measurement [3]. The position labeled with 22 in the 1st quadrant is not well defined in the present prediction.

In Fig. 18, the predicted tip vortex core positions for the

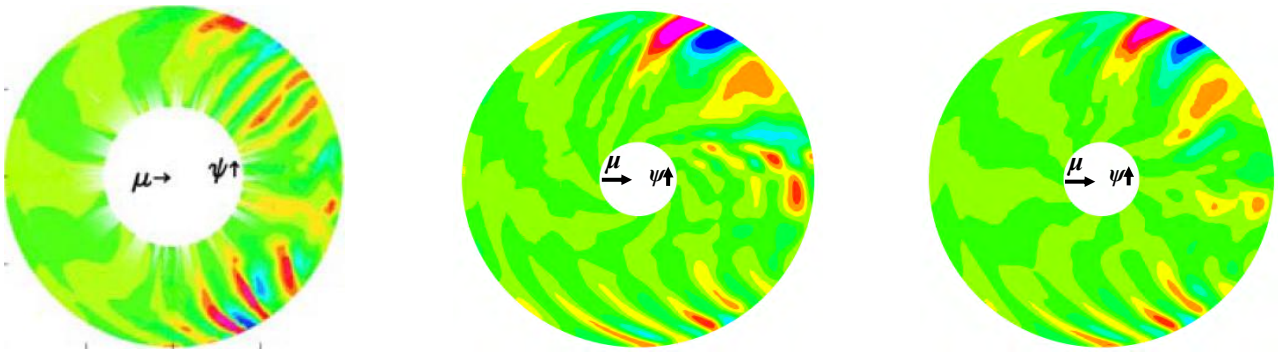

(a) Measurement [3] **(b) Isolated-rotor configuration** **(c) Rotor-fuselage configuration**

Figure 16: Comparison of high frequency components (>7/rev) of leading-edge pressure difference at 3% chordwise position between isolated-rotor and rotor-fuselage configurations after second-level mesh adaptation.

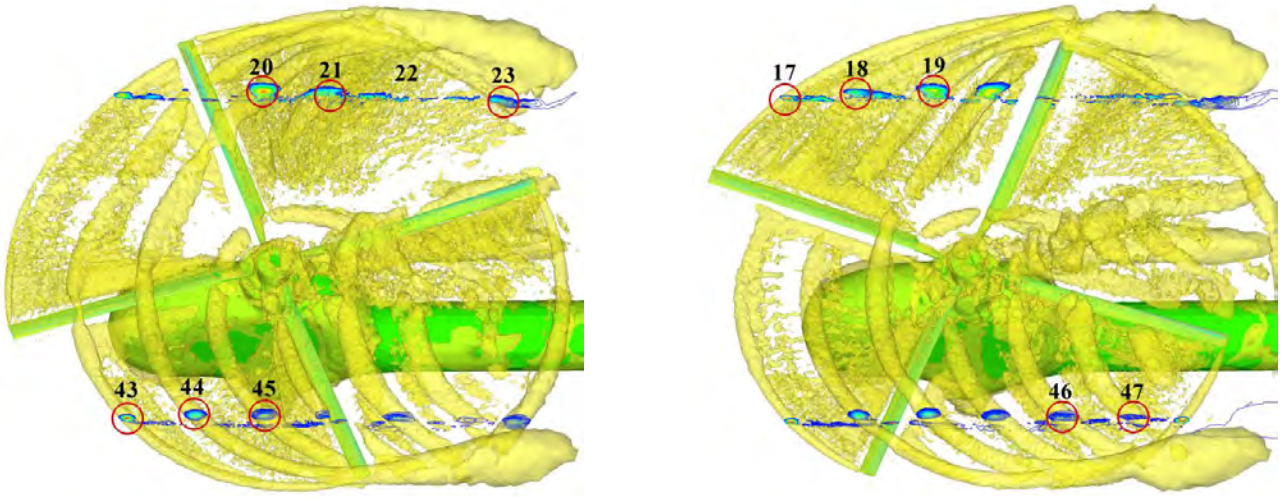

(a) ψ = 20° **(b) ψ = 70°**

Figure 17: Rotor wake structures represented by iso-surface of λ_2-criterion at azimuth angles of 20° and 70° for rotor-fuselage configuration after second-level mesh adaptation.

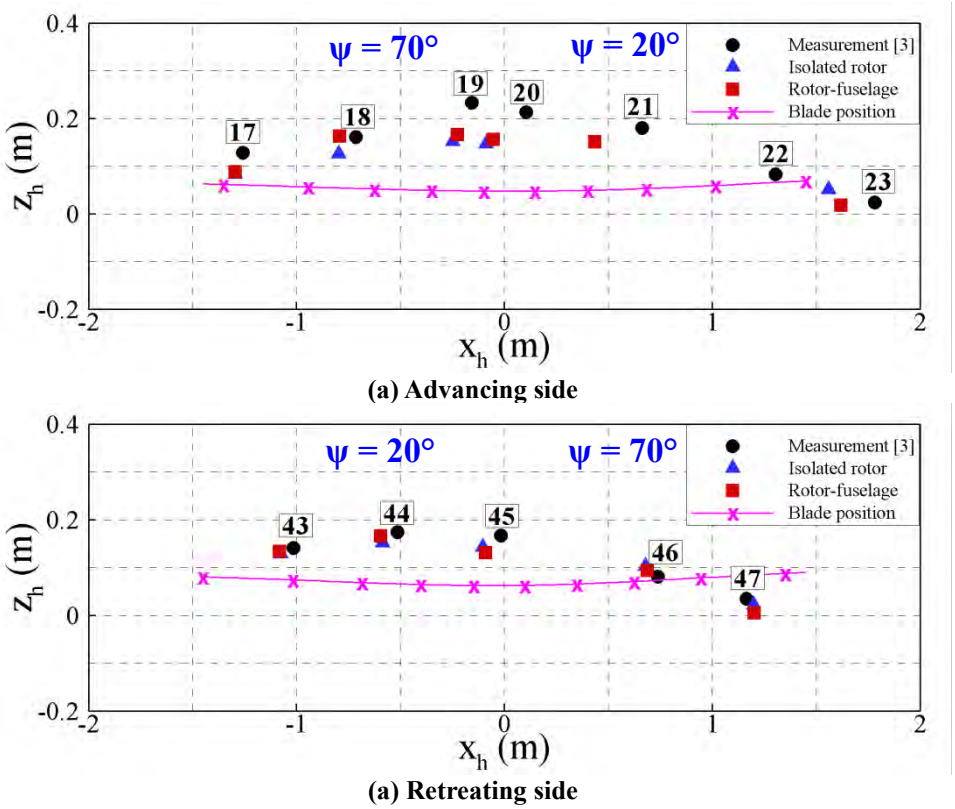

(a) Advancing side

(a) Retreating side

Figure 18: Tip vortex core positions on longitudinal cutting planes at advancing (y=1.4m) and retreating (y=-1.4) sides.

isolated-rotor and rotor-fuselage configurations are compared with the measurement [3]. The core positions correspond to the labeled numbers in Fig. 17. It is shown that both configurations provide reasonable predictions at the retreating side. In contrast, relatively large difference exists at the advancing side, especially in the 1st quadrant where the tip vortex is the oldest. It is also shown that the prediction at the labels 18 and 44 are slightly improved after including the fuselage due to the upwash in the front of the rotor hub. In the figure, the blade position is also presented along with the vortex core positions to indicate the vertical distance between the blade and the vortex cores, which is called the miss distance. This miss distance has the strongest influence on the BVI loading. It is shown that the miss distance at the advancing side is relatively large compared to the retreating side. It is speculated that the large miss distance would make the prediction of high frequency BVI loading more difficult at the advancing side.

7. Conclusions

In the present study, the blade loading and the flow fields around the HART II rotor were numerically investigated using a viscous flow solver on unstructured meshes. A series of solution-adaptive mesh refinement were applied in a quasi-unsteady manner to capture the rotor wake accurately and effectively. A combination of overset mesh and deforming mesh techniques was used to handle the blade motion. The elastic blade deformation was prescribed from the HART II measured data. Calculations were performed for both isolated-rotor and rotor-fuselage configurations. It was found that inclusion of fuselage provides improved predictions for the trim controls and the rotor inflow. This improved trim controls lead to an associated improvement in the prediction of low frequency loading. It was also found that the magnitude of high frequency blade loading caused by BVI becomes more clear as the mesh is further refined, whereas the low frequency loading is mostly independent to mesh adaptation. It was shown that a proper azimuth angle increment, which corresponds to the local cell size, should be used to accurately predict unsteady solutions, such as the high frequency BVI loading. At the retreating side of the rotor, the predicted BVI loading and the wake positions were well matched with the measured data, whereas relatively large discrepancy exists at the advancing side due to the numerical dissipation of the rotor wake.

Acknowledgments

This work was supported by the Human Resources Development of the Korea Institute of Energy Technology Evaluation and Planning (KETEP) grant funded by the Korea government Ministry of Knowledge Economy (20094020100040).

References

[1] Yu, Y. H., Gmelin, B., Heller, h., Philippe, J. J., Mercker, E., and Preisser, J. S., "HHC Aeroacoustics Rotor Test at the DNW – The Joint German/French/US HART Project," 20th Eupopean Rotorcraft Forum, Amsterdam, Netherlands, 1994.

[2] van der Wall, B.G., "2nd HHC Aeroacoustic Rotor Test (HART II) – Part I: Test Documentation," German Aerospace Center Institute Report IB 111-2003/31, 2003.

[3] van der Wall, B. G. and Burley, C. L., "2nd HHC Aeroacoustic Rotor Test (HART II) – Part II: Representative Results, German Aerospace Center Institute Report IB 111-2005/03, 2005.

[4] Lim, J. W., "An Investigation of the Fuselage Effect for HART II Using a CFD/CSD Coupled Analysis," 2nd International Forum on Rotorcraft Multidisciplinary Technology, Seoul, Korea, 2009.

[5] Boyd, D. D., "HART-II Acoustic Predictions Using a Coupled CFD/CSD Method," American Helicopter Society 65th Annual Forum, Texas, USA, 2009.

[6] Biedron, R. T. and Lee-Rausch, E. M., "Rotor Airloads Prediction Using Unstructured Meshes and Loose CFD/CSD Coupling," 26th AIAA Applied Aerodynamics Conference, Honolulu, Hawaii, 2008.

[7] Yang, C. M. and Aoyama, T., "Effect of Computation Parameters on BVI Noise Prediction Using HART II Motion Data," 34th European Rotorcraft Forum, Liverpool, UK, 2008.

[8] Jung, M. S., Kwon, O. J., and Kang, H. J., "Assessment of Rotor Hover Performance Using a Node-Based Flow Solver," KSAS International Journal, Vol. 8, No. 2, 2007.

[9] Kang, H. J. and Kwon, O. J., "Unstructured Mesh Navier-Stokes Calculations of the Flow Field of a Helicopter Rotor in Hover," Journal of the American Helicopter Society, Vol. 47, No. 2, 2002.

[10] Kelly, M., Duraisamy, K., and Brown, R., "Predicting Blade Vortex Interaction, Airloads and Acoustics Using the Vorticity Transport Model," Proceedings of the American Helicopter Society 9th Aeromechanics Specialist Meeting, San Francisco, USA, 2008.

[11] Jung, M. S. and Kwon, O. J., "A Parallel Unstructured Hybrid Overset Mesh Technique for Unsteady Viscous Flow Simulations," International Conference on Parallel Computational Fluid Dynamics, Antalya, Turkey, 2007.

[12] Fahat, C., Degand, C., Koobus, B., and Lesoninne, M. L., "Torsional Springs for Two-Dimensional Dynamic Unstructured Fluid Meshes," Computer Methods in Applied Mechanics and Engineering, Vol. 163, 1998.

[13] Bottasso, C. L., Detomi, D., and Serra, R., "The Ball-Vertex Method: A New Simple Spring Analogy Method for Unstructured Dynamic Meshes," Computer Methods in Applied Mechanics and Engineering, Vol. 197, 2005.

[14] Kholodar, D. B., Morton, S. A., and Cummings, R. M., "Deformation of Unstructured Viscous Grids," AIAA Paper, 2005-0926, 2005.

[15] Yang, Z., Sankar, L. N., Smith, M., and Bauchau, O., "Recent Improvement to a Hybrid Method for Rotors in Forward Flight," AIAA Paper 2000-0260, 2000.